Invasive and minimally invasive optical detection of pigment accumulation in brain cortex

Luís R. Oliveira[1], Tânia M. Gonçalves[2], Maria R. Pinheiro[2], Luís E. Fernandes[3], Inês S. Martins[1,3], Hugo F. Silva[1], Hélder P. Oliveira[4,5], Valery V. Tuchin[6,7,8], and Luís M. Oliveira[1,2]*

[1] Center of Innovation in Engineering and Industrial Technology, ISEP, Rua Dr. António Bernardino de Almeida 431, Porto 4249-015, Portugal

[2] Physics Department, School of Engineering, Polytechnic Institute of Porto, Rua Dr. António Bernardino de Almeida 431, Porto 4249-015, Portugal

[3] Faculty of Engineering, University of Porto, FEUP, Porto 4200-465, Portugal

[4] Institute for Systems and Computer Engineering, Technology and Science, INESC TEC, Porto 4200-465, Portugal

[5] Faculty of Science, University of Porto, FCUP, Porto 4169-007, Portugal

[6] Science Medical Center, Saratov State University, 83 Astrakhanskaya str., Saratov 410012, Russia

[7] Laboratory of Laser Molecular Imaging and Machine Learning, Tomsk State University, 36 Lenin's av., Tomsk 634050, Russia

[8] Laboratory of Laser Diagnostics of Technical and Living Systems, Institute of Precision Mechanics and Control, FRC "Saratov Scientific Centre of the Russian Academy of Sciences", 24 Rabochaya str., Saratov 410028, Russia

* e-mail: lmo@isep.ipp.pt

Abstract. The estimation of the spectral absorption coefficient of biological tissues provides valuable information that can be used in diagnostic procedures. Such estimation can be made using direct calculations from invasive spectral measurements or though machine learning algorithms based on noninvasive or minimally invasive spectral measurements. Since in a noninvasive approach, the number of measurements is limited, an exploratory study to investigate the use of artificial generated data in machine learning techniques was performed to evaluate the spectral absorption coefficient of the brain cortex. Considering the spectral absorption coefficient that was calculated directly from invasive measurements as reference, the similar spectra that were estimated through different machine learning approaches were able to provide comparable information in terms of pigment, DNA and blood contents in the cortex. The best estimated results were obtained based only on the experimental measurements, but it was also observed that artificially generated spectra can be used in the estimations to increase accuracy, provided that a significant number of experimental spectra are available both to generate the complementary artificial spectra and to estimate the resulting absorption spectrum of the tissue. © 2022 Journal of Biomedical Photonics & Engineering.

Keywords: tissue spectroscopy; diffuse reflectance; absorption coefficient; brain cortex; DNA content; blood content; pigment detection; machine learning; generative models.

1 Introduction

Biological tissues differ one from the other in various aspects, since they can have differentiated contents of biological components inside, a different state of health and a different age. The evaluation of such parameters from tissues is not always easy. An example is the evaluation of the tissue state of health in the initial stages of cancer development, since the early-stage formation of cancer cells and the small changes created by those cells

in the surrounding environment are not detected by visual inspection.

Optical methods can help in such evaluations, since any small change in tissue physiology or morphology will translate in changes on the tissue's optical properties [1, 2]. The measurement of the spectral optical properties from similar tissues, such as the refractive index (RI) or the absorption coefficient (μ_a) in a wide spectral range [3] allows to acquire and compare information regarding the contents of proteins, blood and lipids. Detected differences of these contents can be used as bio-optical markers to identify and discriminate pathologies such as cancer [1] or diabetes [4, 5]. Such spectral evaluation also allows to detect the presence of pigments, such as melanin or lipofuscin, whose accumulation in tissues has been reported to be related to the ageing process [6] or to the development of cancer [7, 8]. The evaluation of the scattering coefficient (μ_s), or the reduced scattering coefficient (μ'_s) in a wide spectral range may also be useful to discriminate pathological from healthy tissues. Studies have showed that pathology-induced changes in tissue structure translate in a change of form and magnitude of the μ_s and μ'_s spectra [1, 9].

Considering the potential of the optical methods to acquire diagnostic information, both the RI and the μ_a spectra are sensitive to the absorption bands of tissue chromophores and can be used in the detection of pathology-discriminating information with higher accuracy [10–12]. Considering the identification, quantification and content discrimination of chromophores and pigments between healthy and pathological tissues, the analysis of the spectral μ_a ($\mu_a(\lambda)$) has proven to be more useful [1, 2, 13–15].

The evaluation of $\mu_a(\lambda)$ has been traditionally made through the use of inverse simulations, whose computational codes are based on the Monte Carlo or the Adding-Doubling algorithms [16–18]. These simulation codes require some optical measurements as input, such as the total transmittance (T_t), the total reflectance (R_t), the collimated transmittance (T_c) and the RI of the tissue [16–18]. All these measurements must be acquired from the tissue under study, and although the R_t and RI data can be measured with a noninvasive or minimally invasive procedure from *in vivo* tissues, the T_t and T_c measurements require a more invasive approach and are more commonly made from *ex vivo* tissue samples [19]. Another disadvantage of the traditional simulation methods is that the available codes perform a simulation at a time for individual wavelengths. This means that to acquire the necessary data to reconstruct the $\mu_a(\lambda)$ of a particular tissue for a broad spectral range, one needs to perform a large number of simulations. As recently reported [1, 2, 11, 13–15], such time and computer demanding approach can be replaced by a faster method to calculate the $\mu_a(\lambda)$ of the tissue in a few seconds. This calculation method still needs the T_t and R_t spectra from *ex vivo* tissues, but if those spectra are available, the entire $\mu_a(\lambda)$ can be obtained immediately [1, 13].

To explain this new calculation approach we consider a hypothetical biological tissue sample with slab-form and fixed thickness, d, that consists of a medium where light absorption dominates over light scattering. If this sample is excited by a collimated light beam with intensity $I_0(\lambda)$, then the Bouguer-Beer-Lambert law can be used to calculate the transmitted light intensity, $I(\lambda)$ [13, 20]:

$$I(\lambda) = I_0(\lambda)e^{-A_b(\lambda)}, \qquad (1)$$

where $A_b(\lambda)$ represents the absorbance spectrum of the tissue sample that is defined as [13, 20]:

$$A_b(\lambda) = -ln\left(\frac{I(\lambda)}{I_0(\lambda)}\right) = \mu_a \times d. \qquad (2)$$

Eq. (2) can be used to calculate the $\mu_a(\lambda)$ of the tissue under study from the measured transmitted spectrum. In reality, biological tissues also have significant scattering properties, meaning that a light beam of intensity $I_0(\lambda)$ that irradiates a slab-form tissue sample will be fractioned into three distinct forms, which correspond to the three optical phenomena that occur [19]: light absorption, light transmission and light reflection. Provided that the transmitted light and the reflected light spectral fraction ratios ($T_t(\lambda)$ and $R_t(\lambda)$, respectively) can be measured from the sample, the $A_b(\lambda)$ of the sample can be calculated using the following relation [1, 12]:

$$T_t(\lambda) + R_t(\lambda) + A_b(\lambda) = 1. \qquad (3)$$

The calculation with Eq. (3) is possible for any tissue with dominating absorption, with dominating scattering or with a combination of absorption and scattering properties. The combination of Eqs. (2) and (3) allows to calculate the $\mu_a(\lambda)$ of the tissue from the $T_t(\lambda)$ and $R_t(\lambda)$ that were measured from the slab sample [1]:

$$\mu_a(\lambda) = \frac{1-[T_t(\lambda)+R_t(\lambda)]}{d}. \qquad (4)$$

The measuring setups used to acquire the T_t and R_t spectra use integrating spheres and these ratios are represented in arbitrary units. Consequently, from Eq. (4), $\mu_a(\lambda)$ will be represented in cm^{-1} (or mm^{-1}), depending on the units that d was measured (cm or mm). Although this is a fast procedure to obtain $\mu_a(\lambda)$ of a tissue, it still depends on measurements from excised tissue samples.

Since the main objective of applying optical technologies to clinical practice is to provide efficient diagnostic or treatment approaches that can be made *in vivo*, without excising tissues from the patient, other ways to obtain $\mu_a(\lambda)$ must be searched. One possible approach relies on the acquisition of diffuse reflectance (R_d) spectra, a measurement procedure which can be applied with noninvasive or minimally invasive approaches to *in vivo* tissues [2]. In opposition to the calculations made with Eq. (4), there is no direct relation between the R_d and μ_a spectra. A possible estimation method to reconstruct the $\mu_a(\lambda)$ from spectral R_d measurements relies on the use of machine learning (ML)

techniques and its viability was demonstrated in a recent study with human healthy and pathological colorectal mucosa tissues [2]. Although one of the challenges in the application of ML algorithms in the field of biophotonics is the reduced number of datasets to build the ML models [21], the estimations of the mean μ_a spectra of the colorectal mucosa tissues reported in Ref. [2] were made with acceptable accuracy using only 10 R_d spectra from each tissue. The reconstructed μ_a spectra of both colorectal mucosa tissues were averaged and allowed to obtain discriminated lipofuscin contents in healthy and pathological tissues, showing similar contents to the ones obtained with direct calculations as described by Eq. (4).

The results presented in Ref. [2], although obtained with a small number of datasets to train the algorithms, open the way to apply ML methods to noninvasive tissue spectroscopy measurements for the development of new noninvasive diagnostic procedures. To increase the accuracy of the training process in the development of ML algorithms, a large number of spectra is necessary, but sometimes that is not possible in biophotonics. In some cases, it is not possible to get a large number of tissue samples from different patients or animals to perform the necessary spectral measurements. Another drawback is that for some tissues, no matter how many spectra are measured, they will all be very similar and data variability will be small. New spectra that provide repeated information will be superfluous in the training of ML algorithms and will imply a longer time in the training process. Another option to improve the accuracy of the ML algorithms is to increase the number of available training data by generating new datasets digitally when they are not available experimentally. Such option can be done, but some attention must be made to avoid changing the spectral features, and ensure that the generated spectra are characteristic of the tissue under study. Such artificial generation of spectra can be done using Generative Adversarial Networks (GANs), which is a recent class of ML models that are commonly used to generate new artificial samples of data from a random input [22]. Such procedure is possible since GANs are composed by two distinct ML models, the generator and the discriminator, and they cooperate in a zero-sum game to learn how to generate new synthetic data [23]. The generator model learns how to create new data from random noise and its goal is to fool the discriminator. In contrast, the discriminator will try to differentiate between the generated data and the real experimental data. By the end of the learning process, the generator should be able to artificially create new data that is similar to the already pre-existing experimental data [24]. GANs can be used to generate both new R_d and new μ_a spectra to increase the number of available samples to train and validate other ML models that estimate the μ_a spectra from noninvasive-type R_d spectral measurements. By increasing the available dataset in the algorithms that recreate the μ_a spectra, it is expected that the ML models will become more robust to input variance and avoid overfitting. The use of GANs to increase the number of datasets opens other possibilities,

and such method was used in the present work, as described in Subsection 2.4.

The optical study of brain tissues is of great interest, since the brain is the most complex organ in the body and few studies regarding the spectral optical properties of its tissues have been performed so far. Such interest in the optical studies of brain tissues regards also the high incidence of brain diseases, such as stroke, Parkinson or Alzheimer, in the past 30 years [25]. The ageing process of the brain tissues is directly related to the occurrence of these diseases, since as tissues become older neuron degeneration and death occurs more rapidly [26–28]. To prevent the occurrence of these diseases, a monitoring procedure to evaluate neuron ageing, degeneration and death is most desirable. Optical methods can be used in the development of such procedures, but to do so, the knowledge of the spectral optical properties of the brain tissues in a wide spectral range is necessary. With such knowledge, the development of optical procedures to perform superficial or in-depth monitoring assisted by optical clearing treatments of the health of brain tissues can be possible [19, 29, 30]. Considering such goals to develop new optical methods to monitor tissue's health and ageing in the brain, we performed a study to discriminate and identify the pigment contents in the brain cortex. This study was made using tissue samples from the brain of adult rabbits and consisted on performing spectral measurements to be used both in the direct calculation of the spectral μ_a and in its estimation through ML algorithms. The methodology used in the present study is described in Section 2 and the results are presented in Section 3.

2 Materials and methods

Since the objective of the present study was to obtain and analyze the $\mu_a(\lambda)$ of the brain cortex through different methods, *ex vivo* samples were collected from the brain of rabbits. The selection of the rabbit brain to collect the samples to use in our study was based on that the rabbit and the human brains are very similar, since both have the same three divisions with a fore brain, a mid brain and a hind brain, and also because both contain the cerebellum, the medulla, the corpus callosum, the hypothalamus and the pituitary gland [31].

The research here described is accordingly with the Declaration of Helsinki and was approved by the research review board in biomedical engineering of the Center of Innovation in Engineering and Industrial Technology (CIETI), in Porto, Portugal. Such approval has the number CIETI/Biomed_Research_2021_01. Due to the fact that this study consisted only on the evaluation of the $\mu_a(\lambda)$, both by direct calculation from experimental measurements and by estimation through ML, the following subsections describe the experimental, calculation and estimation procedures adopted.

2.1 Tissue collection and preparation

Ten adult grey rabbits, having a similar age near 36 months, were acquired from a breeder near our lab in

Porto (Portugal), who sells the animals for consumption. The measurements were made with two cortex brain samples from each animal in different days.

For each study with samples from a particular animal, the rabbit was sacrificed in the previous day and the brain was removed from the skull and frozen for 12 h. After this period, tissue samples were sliced from the cortex using a cryostat (Leica^{TM}, Wetzler, Germany, model CM1860 UV). Twenty samples were prepared in total, having an approximated circular form ($\phi \sim 1$ cm) and a fixed thickness of 0.5 mm. All these samples were submitted to spectral measurements, which are described in Subsection 2.2.

2.2 Spectral measurements

To obtain the $\mu_a(\lambda)$ of the brain cortex by direct calculation, two types of spectral measurements were made, using the T_t and R_t setups represented in Fig. 1(a) and in Fig. 1(b). A total number of 10 cortex samples, collected from five adult rabbits, was used to acquire both the T_t and R_t spectra with these setups. These measurements were made in an earlier stage of the research and the corresponding results were already published [13].

At a later stage of the research, other 10 cortex samples were collected from other five adult rabbits and prepared in the same manner to be used in the acquisition of the R_d spectra, which was necessary for the ML estimations. Such measurements were made using the setup presented in Fig. 1(c).
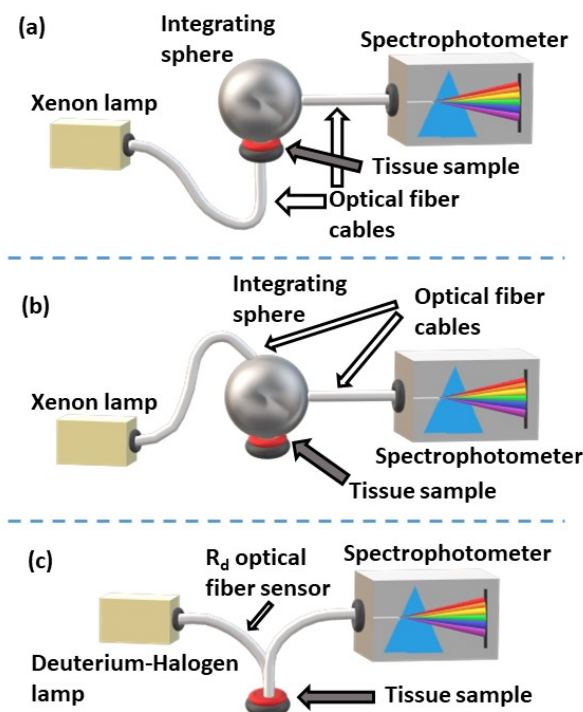

Fig. 1 Experimental setups to measure: $T_t(\lambda)$ (a), $R_t(\lambda)$ (b) and $R_d(\lambda)$ (c).

Considering the measurements with the T_t setup, a broadband pulsed Xenon lamp emits a beam that is delivered below the sample through an optical fiber cable (core diameter of 600 μm). A collimating lens located at the tip of the cable below the sample collimates the beam with a 6 mm diameter. Such beam is transmitted by the tissue sample and then is submitted to several reflections inside the integrating sphere (integration), before being delivered to the spectrometer through a similar optical fiber cable.

Considering the R_t setup presented in Fig. 1(b), the exciting beam that is also emitted by the pulsed Xenon lamp is delivered to an upper entrance of the integrating sphere through an optical fiber cable (core diameter of 600 μm) and collimating lens. The collimated beam with 6 mm in diameter is directed to an exciting direction that makes 8° with the vertical axis of the integrating sphere to guarantee that both specular and diffuse reflectance occur at the tissue surface. After the reflection occurs at the tissue surface, the reflected beam is directed into the inside of the sphere where it is reflected several times at its internal surface (integration), before exiting to be delivered to the spectrometer through a similar optical fiber cable.

In the case of the R_d setup presented in Fig. 1(c), the sample was excited with a broadband deuterium-halogen lamp. An R_d optical fiber sensor, which was kindly supplied by ArtPhotonics^{TM} (Berlin, Germany) for our research, was used both to irradiate the sample and to collect the diffuse reflected light from it. This sensor contained a detection fiber at the center, which was surrounded by seven irradiation fibers, all made of silica with a core diameter of 400 μm and a cladding thickness of 20 μm. The numerical aperture of these fibers was 0.22. The detection fiber at the center was covered with aluminum, having a total diameter of 560 μm. The exciting fibers were covered by polyamide and their total diameter was 465 μm. Such fibers were packed around the detection fiber, without any spacing, having a source-detector separation of 512.5 μm. The tip of the R_d sensor was kept fixed at 2 mm distance above the tissue sample surface during measurements. Apart from the R_d sensor, all the equipment used in the setups presented in Fig. 1 were acquired from Avantes^{TM} (Apeldoorn, The Netherlands).

The reason for using two different lamps in the different measurement setups is that for the case of integrated measurements (T_t and R_t), a high intensity signal is needed for the integration process inside the integrating sphere, and a small intensity signal for the R_d measurements to avoid saturation of the spectrometer. Although two different lamps were used in the T_t / R_t and R_d setups, the spectral measurements in all cases were not influenced by the spectral characteristics of the lamps. For each particular set of measurements, the setup of the spectrometer was made to measure the T_t, R_t or R_d spectra directly. The calculations of these spectra are made by the software of the spectrometer, based on the transmitted or reflected spectra that are measured from the sample and the reference spectra of the lamp used in each setup.

The reflectance reference used both in the R_t and R_d setups was the RS-2 reflectance reference from Avantes, with a reflectance above 92% in the entire spectral range considered in this study.

As referred above, 10 spectra were acquired with each of the setups presented in Fig. 1. These spectra were measured between 200 and 1000 nm. The spectra acquired with the T_t and R_t setups were used in a direct calculation of the $\mu_a(\lambda)$ of the brain cortex, while the spectra acquired with the R_d setup were used as input to the ML algorithms to estimate $\mu_a(\lambda)$ of the brain cortex and compare with the one that results from direct calculations. Subsection 2.3 describes the direct calculations from the experimental measurements, while Subsection 2.4 describes the procedure used in the ML approach.

2.3 Calculations

After performing all spectral measurements with the setups presented in Fig. 1(a) and Fig. 1(b), calculations were made to obtain the $\mu_a(\lambda)$ of the brain cortex. Since 10 spectra were obtained with each measurement setup, 10 μ_a spectra were calculated using Eq. (4). In each of these calculations, a pair of T_t and R_t spectra were used along with the sample thickness, d. Considering the 10 μ_a spectra that resulted from these calculations, the mean $\mu_a(\lambda)$ and corresponding standard deviation (SD) were calculated.

A further analysis of the mean $\mu_a(\lambda)$ showed evidence of pigment content in the brain cortex, meaning that additional calculations were necessary to identify those pigments and discriminate their content. According to literature [32], the brain is known to accumulate mainly melanin and lipofuscin. These pigments originate from their precursors, such as *L*-tyrosine, *L*-cysteine, and dopamine (in the case of melanin) [6] and from cell organelles, such as mitochondria, Golgi apparatus, and lysosomes (in the case of lipofuscin) [33–35]. These precursors can easily associate with metals, specially iron, to form melanin and lipofuscin [36].

Considering that the resulting mean $\mu_a(\lambda)$ that was calculated directly from the experimental measurements represents the mean absorption coefficient of the cortex between 200 and 1000 nm, we looked for the absorption spectra of these pigments on literature. Ref. [37] presents the absorption spectrum of melanin and Ref. [38] presents the absorption spectrum for lipofuscin in the same wavelength range that we considered in our study. We retrieved numerical data from the graphs in these two references and reconstructed the absorption spectra for melanin and for lipofuscin. A graph containing both spectra is presented in Section 3. After obtaining these absorption spectra for the pigments, an optimized combination of both was calculated to subtract to the mean $\mu_a(\lambda)$ of the brain cortex, in a way that such reconstructed absorption presents a horizontal baseline. The results of this calculation and an equation that describes the pigment combination that was used are presented in Section 3.

2.4 Machine Learning estimations

After calculating the $\mu_a(\lambda)$ of the brain cortex directly from the experimental measurements and making an analysis to discriminate the melanin and lipofuscin content in this tissue, another study was made to check if the same results were reachable from a minimally invasive approach.

To proceed with a measuring technique that approaches noninvasive or minimal invasive measurements that can be done *in vivo*, R_d spectra were also acquired from similar tissue samples for the same wavelength range (200–1000 nm). These 10 spectra consist on a reduced number of samples to train the ML algorithms in the reconstruction of the μ_a spectra, but to increase the number of samples to train the algorithms, we first used GANs to artificially generate new R_d and new μ_a spectra from the experimental ones. The objective of this initial process was to turn the ML models that estimate μ_a more robust and decrease their overfitting tendency.

The process of data augmentation with the GANs models consists on the following steps:
a) generate a new artificial spectrum from random noise using the generator,
b) train the discriminator using the both the experimental and the generated spectrum,
c) update the parameters of the generator using the discriminator loss (error metric).

Due to the dynamics between the generator and the discriminator, the GANs model convergence is not a stable state. This happens because there is a certain point in the training process where the generator is so good that the discriminator starts to guess if the new data is real or artificial, which in turn gives the generator deceitful feedback. To prevent this from happening, the training process was stopped when the average of the generated spectra was the closest to the mean experimental data. Another important factor when training GANs models is the learning rate of the generator and the discriminator. As an example, if the discriminator converges earlier than the generator, it increases the chances of model collapse, where the generator only produces one type of sample in an attempt to fool the discriminator. The learning rate was sweep between the 0.001–0.000001 values and then fixed at 0.0001 due to the fact that further decreases did not contribute to a better performance of the GANs model. Additionally, the neural networks that compose the GANs model were defined with different architectures. The discriminator had five layers, being the first two composed with 801 nodes, the third with 600 nodes, the fourth with 400 nodes, and the fifth with 1 node. The generator had five layers, with all the layers having 801 nodes, with the exception of the third, which has only 600 nodes.

During the training process, one of the GANs model was trained to generate new R_d spectra and the other was trained to generate new μ_a spectra. Since these two GANs models converge at different times, the number of epochs for the GANs model that generated new R_d spectra was set to 7901, while the number of epochs for the GANs

model that generated new μ_a spectra was set to 1301. After training and fine tuning of the GANs models, the new generated data was plotted and compared to the experimental data, showing good agreement (presented in Section 3).

After training the GANs models, they were used to generate new spectra in groups of 10, 50 and 100 to train the other ML models in solving the regression problem of recreating the μ_a spectra from the measured R_d spectra. To improve the overall spectral shape of the generated spectra, a Savitzky-Golay filter was applied to smooth the spectra. For each group of generated spectra, three experiments were conducted:

a) in the first experiment, the ML models were trained with the generated spectra and tested with the experimental spectra (G/E),

b) in the second experiment, the ML models were trained with the experimental spectra and tested with the generated spectra (E/G),

c) in the third experiment, both the generated and experimental spectra were combined altogether (AT) to be used in the training and testing of the ML model.

In this last experiment, the generated and experimental spectra were split in an 80/20 proportion to be used in the training and testing procedures to evaluate the performance of the ML model. As an example, for the group of 10 generated spectra, we assured that the test dataset consisted on 8 experimental and 2 generated spectra. A separate experiment was made for the ML model, where no generated spectra were used both in the training and testing process. In this case, the Leave One Out (LOO) method was used to obtain a performance reference point, as we did in our previous work with data from the human colorectal tissues [2].

Similarly to what has been done during the generation of spectra with the GANs models, the Single Layer Perceptron (SLP), the K-Nearest Neighbor (KNN) and the Random Forest Regressor (RFR) algorithms were fine tuned to achieve the best performance possible. These algorithms were the ones with the best performance in our previous study [2]. For this reason, we selected them to use in the present study. The SLP was set with two layers, the first one having 10 nodes and the second having 801 nodes. The learning process was set at 0.001 and the number of epochs was set at 50 during the three experiments that were described above. For the KNN and the RFR algorithms, the number of neighbors and the number of trees where set to 3 and 4, respectively. Further increments in these hyper parameters increase the computational cost of the ML models with no apparent increase in performance.

To quantify the performance of the ML models in the estimation of the μ_a spectra, the Euclidean Distance (ED) between the mean estimated spectrum (MES) and the mean reference spectrum (MRS) was calculated using Eq. (5) [21]:

$$ED = |a - b|, \qquad (5)$$

where a is the μ_a value of the mean estimated spectrum (MES) and b is the μ_a value of the mean reference spectrum (MRS), with the MES calculated from the individual generated spectra and the MRS calculated from the individual experimental spectra.

The results obtained from the GANs and ML estimations and ED comparative graphs to select the best ML algorithm for μ_a generation from the R_d spectra are presented in Section 3. The calculations to retrieve the pigment combination from the $\mu_a(\lambda)$ generated by the best method are also presented to show that pigment content evaluation is possible with a minimally invasive approach.

3 Results

Since the present study was conducted with experimental measurements to obtain the $\mu_a(\lambda)$ of the brain cortex, both by direct calculation and through ML estimations, the presentation of results is divided in various subsections. Subsection 3.1 presents the mean experimental spectra that were used in the various stages of this study. Subsection 3.2 presents the results obtained with the direct calculation approach and Subsection 3.3 presents the results estimated through ML. Subsection 3.4 presents the evaluation of the pigment content, both from the direct calculation and from the ML estimation approaches.

3.1 Spectral measurements

The first step of the present study consisted on acquiring spectral measurements with all the setups in Fig. 1. As indicated in Subsection 2.2, 10 T_t and 10 R_t spectra were acquired from 10 cortex samples at an initial stage. At a later stage 10 R_d spectra were acquired from 10 similar cortex samples. The samples used in these measurements were all collected from adult rabbits acquired from the same supplier. The mean and SD of the T_t, R_t and R_d spectra that resulted from these measurements are presented in Fig. 2.

The wavelength dependencies for all mean spectra presented in Fig. 2 are accordingly to others previously obtained from other biological tissues [1, 2, 12, 14, 15]: T_t increases with the wavelength and both R_t and R_d decrease with the wavelength. All mean spectra in Fig. 2 present good sensitivity to the absorption bands of DNA/RNA (260 nm) and hemoglobin/myoglobin (274, 415, 540 and 570 nm). The mean T_t spectrum also shows evidence of water in the tissues – absorption band centered at 980 nm.

Regarding the SD, the R_d spectrum presented in Fig. 2(c) shows small magnitude (less spreading between samples in these measurements) for the entire spectral range. In the case of the T_t spectrum, SD is very low for shorter wavelengths due to the strong absorption between 200 and 300 nm, while for longer wavelengths it increases with the wavelength. The R_t spectrum presents a more or less constant SD in the entire spectral range.
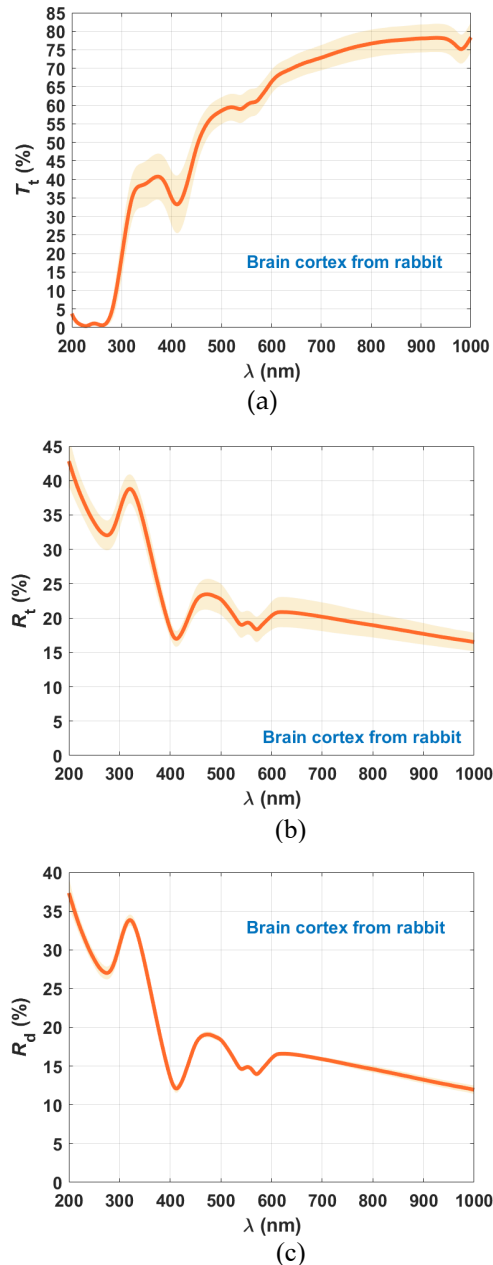
(a)

(b)

(c)

Fig. 2 Mean measured spectra and SD of the rabbit brain cortex: (a) $T_t(\lambda)$, (b) $R_t(\lambda)$, and (c) $R_d(\lambda)$.

3.2 Direct calculation of $\mu_a(\lambda)$

Using the T_t and R_t spectra two by two in Eq. (4), the 10 μ_a spectra were calculated. The mean $\mu_a(\lambda)$ and SD that resulted from these direct calculations are presented in Fig. 3.

Due to the contributions of T_t and R_t in the calculation of the $\mu_a(\lambda)$ through Eq. (4), there are several absorption bands visible in Fig. 3. The first absorption band occurs at 230 nm, showing the amino acid connections of tyrosine and tryptophan in proteins [39, 40]. The occurrence of this band is not surprising, since it is known that the brain tissues, especially the cortex contain several types of proteins, such as actin, albumin, α-tubulin, β-tubulin, neuron specific enolase (NSE), and

vimentin [41]. The second absorption band seen in Fig. 3 occurs at 267 nm, showing a combination of the absorption band of DNA/RNA at 260 nm with the one of hemoglobin at 274 nm [42]. The absorption bands of oxygenated hemoglobin in the visible range are also visible at 411 nm (Soret band) and 540 and 570 nm (Q bands) [42], as well as the absorption band of water at 980 nm [42].
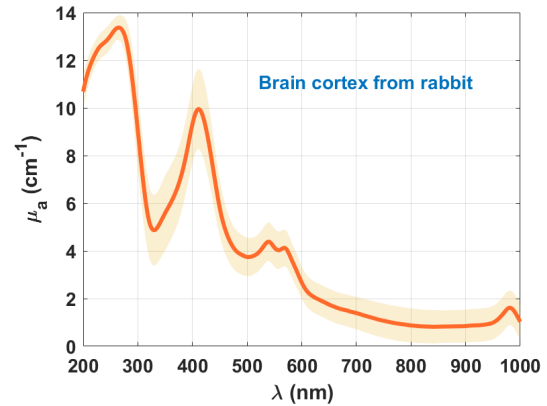

Fig. 3 Mean μ_a spectrum and SD of the rabbit brain cortex.

Additional information can be retrieved from the mean $\mu_a(\lambda)$ represented in Fig. 3, since such spectrum presents a decreasing baseline with increasing wavelength. Such behavior for the baseline suggests the presence of pigments in the cortex brain tissues that were used in the present study. A further analysis of this spectrum will be made in Subsection 3.4 to identify the pigments and quantify their content. First, we need to check if the ML estimations are capable of generating similar $\mu_a(\lambda)$ from the R_d spectra as the ones obtained with direct calculation from invasive measurements. Such part of the study is presented in Subsection 3.3.

3.3 Machine Learning estimation of $\mu_a(\lambda)$

Once the $\mu_a(\lambda)$ of the brain cortex was calculated directly from the experimental spectra of T_t and R_t, we initiated the estimation of the absorption spectrum through ML algorithms. According to the description presented in Subsection 2.4, this part of the study was initiated by training and fine-tuning the GANs models to generate both new R_d and μ_a spectra to be used for the training and validation of the ML algorithms. After fine-tuning the GANs, the new generated spectra were represented along with the experimental spectra in Fig. 4 for comparison.

As we can see from graphs in Fig. 4, some low-magnitude discrepancies are seen between the ME and the MG spectra at some wavelengths. Regardless of these discrepancies, the overall wavelength-dependence and the magnitude of the generated spectra are very similar to the ones that result from direct calculations with the experimental measurements. After this initial training and tuning of the GANs, they were used to generate new groups of 10, 50 and 100 spectra. Such groups of spectra were used in the training process of the ML algorithms to

recreate $\mu_a(\lambda)$ from $R_d(\lambda)$, as described in Subsection 2.4. Such training process was made in four ways – using only the 10 experimental spectra with the LOO method, using 10 experimental and 10 generated spectra, using 10 experimental and 50 generated spectra, and using 10 experimental and 100 generated spectra. By doing these different trials, we expect to identify both the overfitting and the underfitting characteristics of the ML algorithms and also to see if the increase of the generated spectra prevents the occurrence of the overfitting. Such four tests were made with all ML algorithms.

(a)

(b)
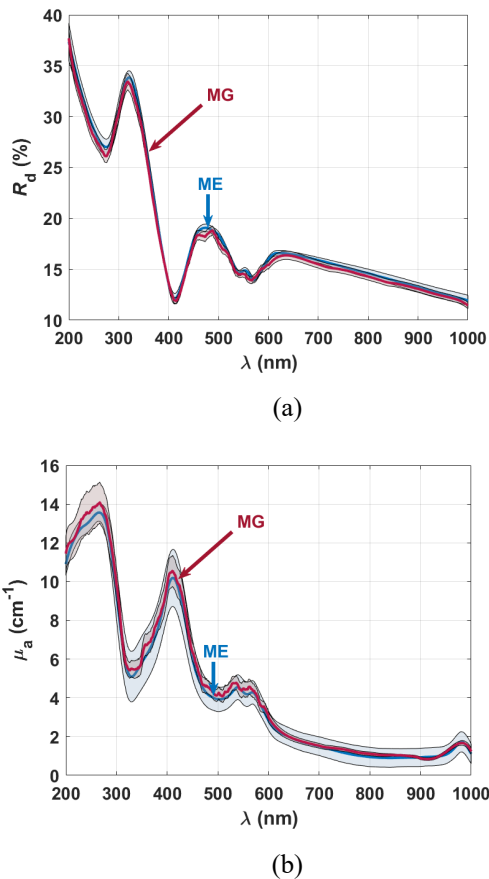
Fig. 4 Mean experimental (ME) and mean generated (MG) spectra for R_d (a) and μ_a (b) of the rabbit brain cortex.

The first ML algorithm that was used to recreate $\mu_a(\lambda)$ from the $R_d(\lambda)$ was the SLP. The second was the KNN and the third was the RFR. Following the estimation procedure described in Subsection 2.4, in all AT estimations with each algorithm, the spectra generated with the GANs were combined with the experimental spectra, having 80% of the total spectra been used in the training process and the remaining 20% been used in the validation process of the algorithm. Experimental spectra were included both in the training and in the validation process of the three AT algorithms.

To evaluate which algorithm generated the better μ_a spectra, Eq. (5) was used to calculate the ED as a measurement of the algorithm performance. Fig. 5 presents the results of these calculations for four cases,

according to the number of generated spectra used in the estimations: none, 10, 50 and 100.
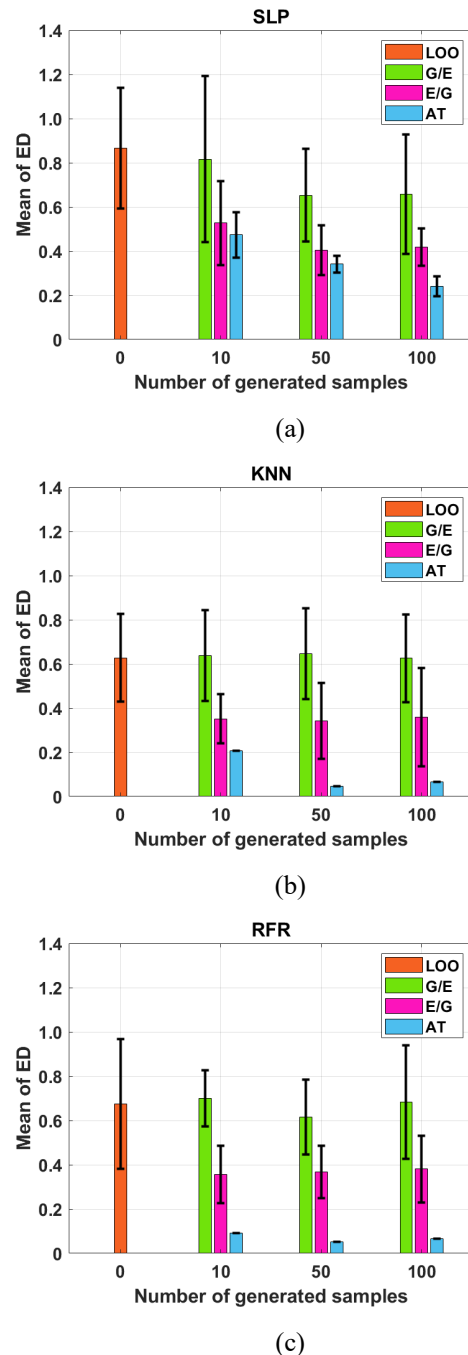

(a)

(b)

(c)

Fig. 5 Calculated ED for the SLP (a), the KNN (b) and the RFR (c) models.

Analyzing the graphs in Fig. 5, we see various information. First, the ED obtained for the LOO method presents a high value for all algorithms, indicating that by using only 10 experimental spectra, the estimations are deceiving. Considering the SLP algorithm, we see that the G/E method shows similar ED for 10 generated samples to the one observed for the LOO method. By increasing to 50 generated samples, a decrease of the mean ED is observed, but no improvement is seen when

the number of generated samples increases to 100. Considering the E/G method, when 10 generated samples are used in the training process, we see a significant decrease of ED from the one obtained for the LOO method. When 50 generated samples are used, a further decrease is observed, but increasing the number of samples to 100, no improvement is observed, once again. The AT method is the one that presents a continuous decrease of ED in the SLP algorithm, but comparing with the other algorithms, the SLP is the one that presents the highest SD values.

In the case of the KNN the ED value obtained for the G/E method remains almost equal to the one obtained with the LOO method in all cases tested. This means that such method does not show any improvement in the recreation of μ_a. The E/G method presents similar variations to the ones observed with the SLP algorithm, but with a higher SD. Once again no improvement is seen when passing from 50 to 100 generated samples. The AT method is the one that presents higher decreases of ED in all cases studied with the KNN algorithm. In this study, very low mean ED and SD values are seen for the cases of 50 and 100 generated samples. Although these values are low, the mean ED for the study with 10 generated samples is still comparably high.

Finally, when using the RFR algorithm, we see variations for the mean ED that are similar to the ones obtained for the KNN algorithm. Considering the magnitude of the SD, and with the exception of the G/E estimation with 100 generated samples, we see smaller values than in the other algorithms. In the case of the G/E, once again the mean ED remains almost unchanged and similar to the value obtained for the LOO method. The ED for the E/G method decreases to about one-half of the value seen for the LOO method, but no improvement is seen when the number of generated samples is increased. In the case of the AT method, we see the best results, since in all cases tested with this algorithm, a significant decrease is observed, obtaining ED values always below 0.1.
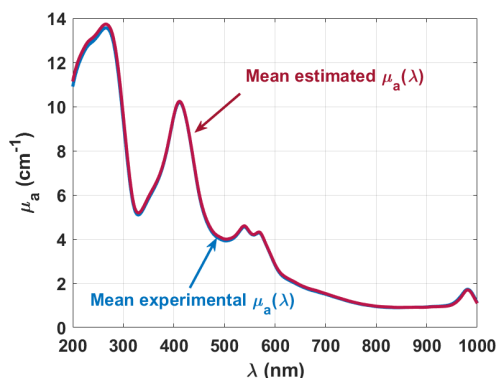
Fig. 6 Comparison between the MES and the MRS of μ_a that result from the estimation with the LOO method.

An overall evaluation of the results presented in Fig. 5 shows that the RFR algorithm is the one with the best performance. Not also it presents the highest decrease in

ED for the AT method, but all estimation methods tested with this algorithm present the lowest SD. Considering these facts, we represented in the following four figures all the MES obtained with the RFR algorithms to compare with the MRS that resulted from the direct calculations, as presented in Fig. 3. Such comparison is made in Fig. 6 for the MES obtained with the LOO method, in Fig. 7 for the MES obtained with 10 generated spectra, in Fig. 8 for the MES obtained with 50 generated spectra and in Fig. 9 for the MES obtained with 100 generated spectra.
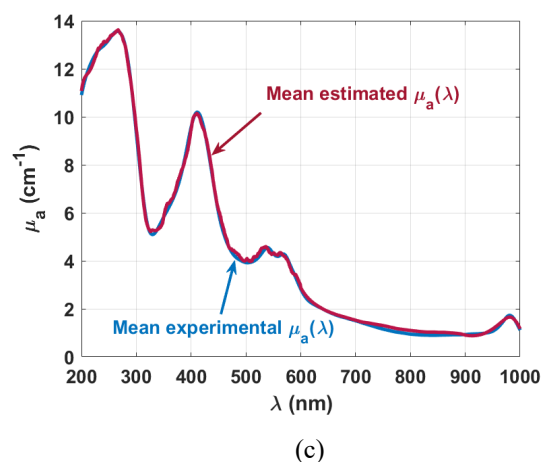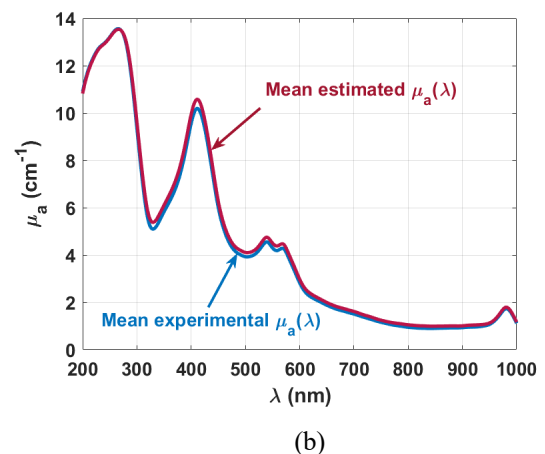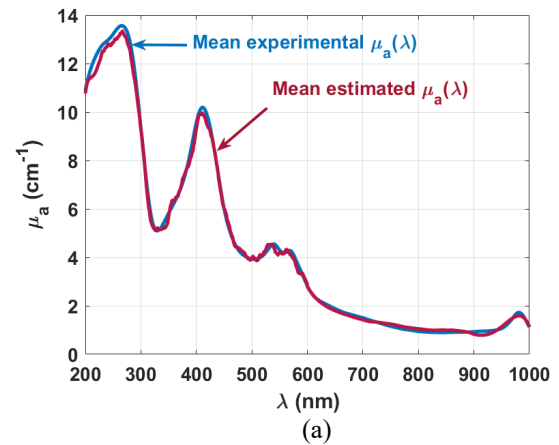
Fig. 7 Comparison between the MES and the MRS of μ_a that result from the estimations with 10 generated samples: 10–G/E (a), 10–E/G (b) and 10–AT (c).
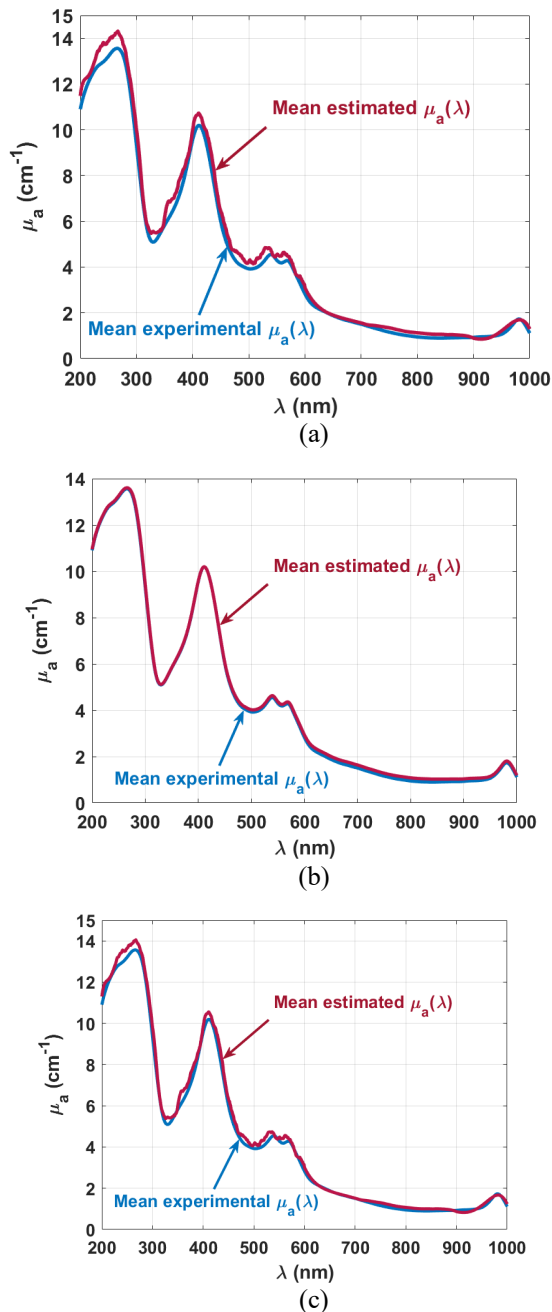
Fig. 8 Comparison between the MES and the MRS of μ_a that result from the estimations with 50 generated samples: 50–G/E (a), 50–E/G (b) and 50–AT (c).

Considering the matching of the MES to the MRS in the various panels presented in the above Figs., we see that in general they are all good, presenting the same levels of μ_a at all wavelengths, similar wavelength dependencies and showing the same absorption bands. The best matching is obtained for the LOO method (Fig. 6), but such good matching is deceiving, since only a small number of experimental spectra were used both in the training and in the validation of the RFR model to obtain such mean estimation. Other good estimations that apart from the previously mentioned characteristics show good spectral smoothing are the ones obtained with the E/G method (see Figs. 7(b), 8(b) and 9(b)). Although

these estimations are only second-best to the one obtained with the LOO method, once again these results are also deceiving. By using the experimental spectra in the training process and the generated spectra in the validation is not a reliable approach in the ML point-of-view. Nevertheless, the analysis of the corresponding graphs in the above Figures shows that this method also improves with the increase of the generated spectra that are used in the validation. When we analyze the mean estimations produced by the G/E method (see Figs. 7(a), 8(a) and 9(a)), we see that the mean estimations lose the smoothing characteristic. Regardless of the lack of spectral smoothing, these estimations also show good agreement with the MRS in terms of wavelength dependence, μ_a levels and absorption bands. Comparing between the three estimations with the G/E method, we see that the worst case occurs for the estimation with 50 generated spectra. Such result shows that if a large number of experimental spectra were available in the GANs generation process, a better performance could be obtained with this method. Finally, the MES obtained with the AT method also shows lack of spectral smoothing (see Figs. 7(c), 8(c) and 9(c)), but the μ_a spectra obtained with this method are more approximated to the MRS, as indicated by the lowest ED values in the graph in Fig. 5(c). Once again, the results obtained with the AT method show that more experimental spectra are necessary to improve both the generation of new spectra with the GANs models and the estimation of the $\mu_a(\lambda)$ from the measured $R_d(\lambda)$.

The data in the graphs of Figs. 6, 7, 8 and 9 show the necessity of increasing the number of samples to use in the training and validation of the ML algorithms to improve the quality of the estimations. Such increase in the number of experimental spectra would also improve the efficiency of the GANs to generate new spectra. By doing that, the various estimations presented in the previous Figures could have higher spectral smoothness, which is the most evident flaw in the estimations made with the G/E and AT methods. Nevertheless, if we disregard the lack of smoothness in the estimated spectra, we see from the previous Figures that all cases studied present acceptable results. We will now present the final stage of this research – the evaluation of pigment content in the brain cortex.

3.4 Pigment content evaluation from the calculated and estimated $\mu_a(\lambda)$

After performing an evaluation on the quality of the $\mu_a(\lambda)$ that were estimated with the various methods within the RFR algorithm, we will now consider the ones that presented the best performance for the further calculations to obtain the pigment content in the brain cortex. At this last stage of the research it will be interesting to check if the estimated μ_a spectra have similar contents of melanin and lipofuscin, and if by retrieving the absorption of those pigments we can find similar absorption ratios for DNA/RNA and hemoglobin as the ones previously obtained for the $\mu_a(\lambda)$ that was

obtained from direct calculation [13]. Although the tissue samples used to acquire the spectral measurements for the direct calculation and for the ML estimations of $\mu_a(\lambda)$ were collected from different animals, those animals were obtained from the same source and were all adults with approximately the same age.
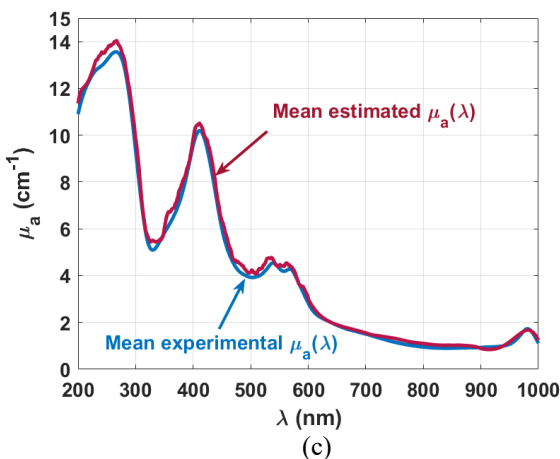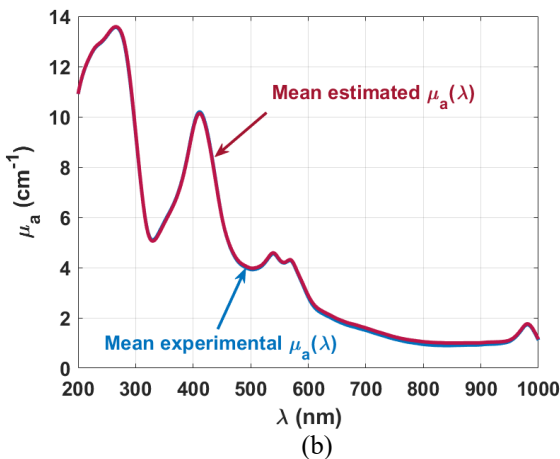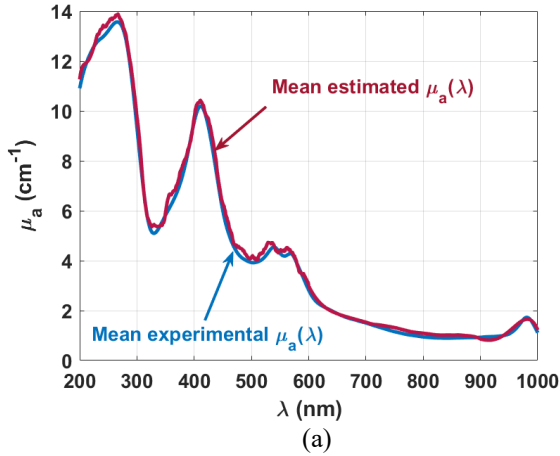

(a)

(b)

(c)

Fig. 9 Comparison between the MES and the MRS of μ_a that result from the estimations with 100 generated samples: 100–G/E (a), 100–E/G (b) and 100–AT (c).

In the same way as we did with the $\mu_a(\lambda)$ obtained with direct calculations [13], we started by reconstructing the absorption spectra of melanin and lipofuscin from graphical data published in literature [37, 38]. These spectra are presented in Fig. 10.
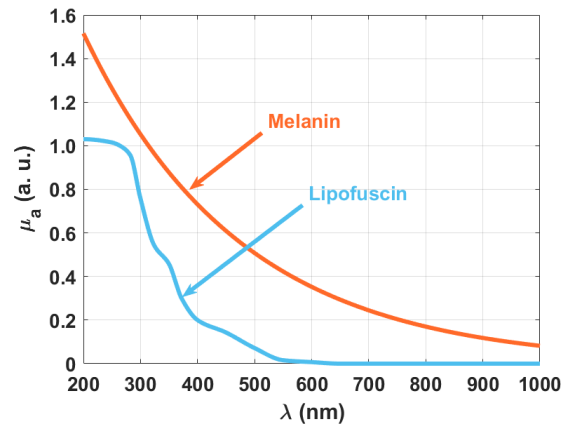

Fig. 10 The absorption spectra (μ_a) for melanin and lipofuscin.

The absorption spectrum of melanin presented in Fig. 10 was reconstructed from graphical data presented in Ref. [37] and it correspond to eumelanin, the most common type of the melanin pigments, and the one that can be observed in the skin. The authors of Ref. [37] constructed such graph based on diffuse reflectance measurements made from human skin *in vivo*, but in that paper it is also indicated that such data does not differ much from the one collected from *ex vivo* samples. In the case of the melanin found in brain tissues, which is commonly designated as neuromelanin, it is a mixture of eumelanin and pheomelanin [43]. With the objective of reconstructing the absorption spectrum of neuromelanin with the highest precision, we searched for the absorption spectrum of pheomelanin to see if it differs from the one of eumelanin that is reported in Ref. [37]. A discussion of the extinction coefficient both of eumelanin and pheomelanin is available on the website of the Oregon Medical Laser Center [44], where both types of melanin present a very similar extinction spectrum between 200 and 900 nm. Since these spectra are very similar, by considering in our study the spectrum of eumelanin, as represented in Fig. 10, we can consider that it is a good approximation to the mixture of eumelanin and pheomelanin that composes the neuromelanin in the brain tissues.

Since the absorption spectra presented in Fig. 10 were reconstructed from published graphical data, no mathematical equation is available to describe them. This means that to combine these spectra with the objective of subtracting such combination from the $\mu_a(\lambda)$ of the brain cortex, numerical data for each of the curves in Fig. 10 needs to be considered. In the case of the $\mu_a(\lambda)$ that was obtained through direct calculations [13], and after some trials to combine the two spectra in Fig. 10 to characterize the pigment content in the cortex, we found that such content is characterized by the following combination:

$$\mu_{a-\text{pigment}}(\lambda) = 3.5 \times M(\lambda) + 1.9 \times L(\lambda), \quad (6)$$

with $M(\lambda)$ and $L(\lambda)$ representing the wavelength dependencies of the absorption coefficient of melanin and lipofuscin, respectively, as represented in Fig. 10.

As referred in Ref. [13], Eq. (6) provides a good description of the decreasing baseline that is seen in Fig. 3, but such baseline may not be only due to the presence of these pigments in the cortex. The precursors of these pigments or other pigments may also be included in the cortex and contribute to the absorption baseline. An example is hemosiderin, which has an absorption spectrum similar to the one of melanin [45]. Since the cortex tissues used in the present study presented no evidence of rapid hemoglobin destruction or fast and excessive iron deposition, we neglected the absorption of hemosiderin in the calculation of $\mu_{a\text{-pigment}}(\lambda)$ with Eq. (6). Considering carotenoid-type pigments, such as lutein, β-cryptoxanthin, and zeaxanthin, all have a similar absorption spectrum, with null absorption for wavelengths above ~500 nm and low absorption in the UV range. Between 400 and 500 nm, these carotenoid-type pigments have three absorption peaks, being the higher magnitude of these peaks observed for β-cryptoxanthin [46]. Due to the fact that these absorption bands occur between 420 and 476 nm [46], they seem to have no influence in the resulting $\mu_a(\lambda)$ of the cortex. As seen in Fig. 3 for this wavelength range, the mean μ_a spectrum of the cortex only shows a well-defined Soret band, with center wavelength at 411 nm.

Considering the melanin precursors, they show an absorption spectrum mainly characterized by UV-bands, with null values above 300 nm. L-cysteine, has an absorption spectrum which consists on the combination of two overlapping bands, the one with higher magnitude centered near 230 nm and the other centered near 280 nm [47]. This means that L-cysteine might also be present in the brain cortex tissues and that its absorption may contribute to the absorption band that we see at 230 nm in Fig. 3. The absorption spectrum presented in Fig. 3 shows no evidence of the 280 nm band, but the strong band at 267 nm that results from the combination of the DNA/RNA band at 260 nm and the hemoglobin band at 274 nm, might be masking the 280 nm band. Considering L-tyrosine, its absorption spectrum is the combination of two bands with a small overlapping, with the higher-magnitude band being centered at a wavelength smaller than 240 nm and the other centered near to 285 nm [48]. Considering dopamine, its absorption spectrum contains only a single band, with a central peak near 280 nm [49]. As in the case of L-cysteine, and for the same reasons presented above, the absorption bands of L-tyrosine and dopamine may be masked by the strong absorption bands of the amino acid connections in proteins and the one that results from the combination of DNA/RNA and hemoglobin. Such fact suggests that melanin precursors may also be present in the cortex samples used in the present study.

Considering now the lipofuscin precursors, we found only the absorption spectrum for mitochondria, which is also limited to the UV range. Such spectrum contains a single band between 300 and 400 nm, with the peak near 360 nm [50]. Considering the absorption spectrum that we calculated for the brain cortex (Fig. 3), the absorption band of mitochondria may be masked by the Soret band, which extends to a lower wavelength close to 320 nm.

Considering the above discussion about the absorption spectra of pigments and their precursors, and assuming that only melanin and lipofuscin contribute to the decaying baseline presented in Fig. 3 for the brain cortex, we will now present a comparative evaluation of the pigment contents in the various $\mu_a(\lambda)$ that were estimated by the different RFR methods used in the present study. The first step of this final comparative study consisted on subtracting the combination of melanin and lipofuscin absorption, as described by Eq. (6), from the mean μ_a spectrum presented in Fig. 3. The corrected $\mu_a(\lambda)$ obtained with this calculation is considered as a reference for the similar calculations to be made with the different μ_a spectra that were generated with the best performance methods with the RFR model. Such methods are the AT with 10, 50 and 100 digitally generated spectra, as presented in Fig. 5. We also considered the spectrum generated with the LOO method to evaluate its capability with a low number of experimental spectra to reproduce the pigment content and evaluate the DNA and hemoglobin ratios. In these calculations, the combination of pigments to subtract to each mean μ_a spectrum was recalculated as in Eq. 6, but using different numbers as multiplication factors to $M(\lambda)$ and $L(\lambda)$, so that the corrected $\mu_a(\lambda)$ could have similar baseline values to the ones that were obtained from the corrected $\mu_a(\lambda)$ that results from direct calculations. The results from these calculations are presented in Fig. 11 for the cases of direct calculations from experimental measurements and the LOO method.

Comparing between the two graphs of Fig. 11, it is seen that the μ_a spectra that result from direct calculations and from the LOO method (blue curves) are very similar. The corresponding μ_a spectra that were obtained using the AT method with 10, 50, and 100 digitally generated spectra are also similar to these, but some small differences exist. As an example, comparing between the two graphs of Fig. 11, it is seen that the absorption peaks at 267 and 411 nm are a little higher in the case of the LOO method than in the case of direct calculations.

The double-arrow lines presented in both graphs of Fig. 11 refer to the calculated ratios at the main absorption bands, with center wavelengths at 267 nm, 411 nm and 550 nm. Before subtracting the pigments, those ratios were calculated as the value of μ_a in the blue curve divided by the value of μ_a of the pigment in the pink curve. After subtracting the pigment absorption (pink curve) to the μ_a of the brain cortex (blue curve), the corrected μ_a spectrum of the brain cortex (green curve) was obtained in all cases studied. Considering such corrected spectra, the new ratios were calculated as the value of μ_a at the above wavelengths in the green curve divided by the minimum value in that same curve, which occurs at 801 nm and is represented by the black horizontal line in both graphs of Fig. 11.
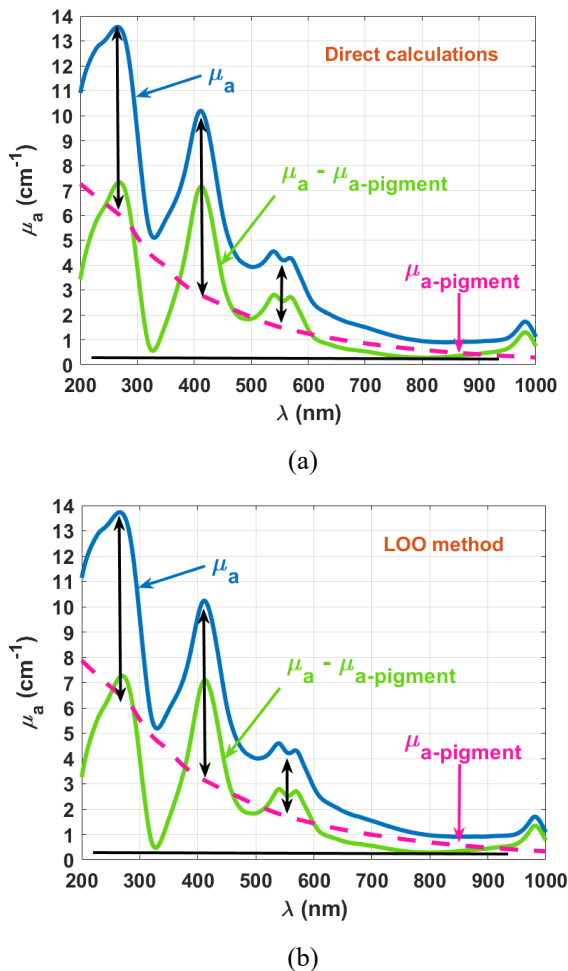
(a)

(b)

Fig. 11 Wavelength dependencies of μ_a for the combination of melanin and lipofuscin and for the rabbit brain cortex, before and after subtracting the absorption of the pigments that resulted from direct calculations (a), and RFR-LOO estimation (b).

To summarize the calculations performed to obtain the pigment contents and the results presented in Fig. 11, Table 1 contains the melanin and lipofuscin combinations used in each case.

Table 1 Pigment combinations used in the various methods to obtain the corrected $\mu_a(\lambda)$ of the brain cortex.

Method	Pigment content
Direct calculation	3.50×M+1.90×L
RFR – LOO	4.04×M+1.70×L
RFR – 10AT	4.84×M+0.40×L
RFR – 50AT	4.68×M+1.00×L
RFR – 100AT	4.85×M+0.60×L

Considering the multiplication factors for M and L in Table 1, we see that all methods studied show a higher content of melanin than the one of lipofuscin in the brain cortex. Although the ML models used in the present study showed some drawbacks, they were all able to reach the same result that differentiates the melanin and lipofuscin contents in the brain cortex. Comparing between methods, the multiplication factors in Table 1 show that both the LOO and the AT methods originate a higher content of melanin and a lower lipofuscin content than the ones obtained through the direct calculation method.

To evaluate the DNA and hemoglobin contents in the brain cortex, the absorption ratios at the main absorption bands were calculated for all methods, before and after subtracting the pigments absorption from the μ_a spectra. Table 2 presents those results at the wavelengths 267 nm, 411 nm and 550 nm for comparison.

Table 2 Absorption ratios for the main absorption bands of DNA and hemoglobin for the various methods used to obtain $\mu_a(\lambda)$ of the brain cortex.

	Absorption ratios at central wavelengths					
	267 nm		411 nm		555 nm	
Method	before	after	before	after	before	after
Direct calculation	2.19	26.42	3.55	25.80	2.73	9.26
RFR – LOO	2.12	26.23	3.25	25.64	2.50	9.10
RFR – 10AT	2.22	27.11	2.92	24.18	2.11	8.07
RFR – 50AT	2.15	27.12	3.04	25.61	2.25	8.81
RFR – 100AT	2.21	27.92	2.99	25.39	2.17	8.62

Considering the data presented in Table 2, we see that the LOO method produces very close ratios to the ones obtained with the direct calculation method for the considered absorption bands. In order to reach these values, a higher melanin content and a lower lipofuscin content needed to be considered to reproduce the corrected $\mu_a(\lambda)$ that results from the ML-LOO method. By reaching these results with a limited number of experimental spectra, the LOO method can be considered a good option to recreated the μ_a spectrum, but with limited statistics, as explained in our previous study [2].

When introducing artificially generated spectra with the objective of obtaining higher performance for the RFR algorithm, we see that by increasing the number of digital spectra from 10 to 50 and then to 100, all studies show absorption ratios in the same order of magnitude of the ones obtained in the direct calculation procedure. As the number of digital spectra increases from 10 to 50, we see that the absorption ratios become more approximated to the ones obtained through the direct calculation approach, but when considering 100 digital spectra, such approximation becomes worse. Such variation indicates that the GANs models used to generate digital spectra work to a certain point, and if the number of generated spectra increases above some limiting value, the generated spectra present features that differ from the real tissue under study. This occurs due to the fact that the GANs models learn the normal distribution of the experimental spectra. Consequently, when the number of artificially generated spectra is increased above a certain limit, the GANs models are more likely to generate low-quality spectra that are located at the extremes of the

normal distribution. Considering the GANs models used in this study to generate both the R_d and μ_a spectra, the generated data seems to maintain the spectral quality up to a number of 50 digitally generated spectra. Such spectral quality is not maintained for a higher number of artificially generated spectra, as we observed in some trials that were performed. In future applications we plan to use different GANs models to generate spectra artificially and fine-tuning will be performed to obtain a significant number of artificial data.

4 Conclusions

The present study shows the possibility of using ML estimations to reconstruct the $\mu_a(\lambda)$ of a tissue from noninvasive or minimally invasive spectral measurements, but to obtain high accuracy in the estimated spectra, a large number of experimental spectra is necessary. When a large number of measured spectra is not available, which is the most common case in spectral biophotonics, and if the LOO approach is acceptable for a particular study, it can be used to recreate $\mu_a(\lambda)$ and obtain diagnostic information with good accuracy. In cases when the LOO method is not an option, and the artificial generation of spectra is a possibility, the RFR or other algorithms can be used to recreate $\mu_a(\lambda)$. In that case, the digital generation of spectra can be made using GANs, but this study shows that a small number of experimental spectra will not be sufficient to generate a large number of artificial spectra with good quality. To obtain such high numbers of good artificial spectra, a considerable number of experimental measurements must be provided.

To evaluate the precision of the algorithms and models used in our study, the mean ED between the MES and MRS was calculated. Since the LOO method uses only experimental spectra, we considered its mean ED as a reference in the evaluation of the other methods accuracy. As reported in the graphs of Fig. 5, the LOO method had a mean ED of 0.628.

Considering the different methods used with the SLP algorithm, and retrieving data from Fig. 5(a), for the studies, where 10, 50 and 100 digitally generated spectra were used, the mean ED values obtained were: 0.817, 0.652 and 0.658 with the G/E method; 0.527, 0.404, and 0.418 with the E/G method; and 0.474, 0.341, and 0.241 with the AT method.

In the studies performed with the KNN algorithm, the mean ED values obtained with 10, 50 and 100 digitally generated spectra were: 0.638, 0.647, and 0.625 with the G/E method; 0.352, 0.343, and 0.360 with the E/G method; and 0.206, 0.048, 0.067 with the AT method.

The last algorithm used in our study was the RFR. For the studies with this algorithm with 10, 50, and 100 digitally generated spectra, the mean ED values obtained were: 0.701, 0.616, and 0.684 with the G/E method; 0.357, 0.367, and 0.381 with the E/G method; and 0.092, 0.052, and 0.066 with the AT method.

Analyzing all these accuracy values, we see that the G/E method provides the worst results, always above the one obtained with the LOO method. Both the E/G and the AT methods provide better results than the LOO method in all algorithms, but considering all the studies performed, the AT method is the best. Considering this method, the mean ED values obtained both with the KNN and with the RFR algorithms can be considered the best of the whole study.

After evaluating the limitations on the application of ML methods in spectral biophotonics to estimate tissue absorption, we intend to perform other studies in the future with a biological tissue where a large number of measurements is possible. We expect that by performing such studies and obtaining a significant number of R_d and μ_a spectra for a particular tissue, we can use GANs models to generate a high number of artificial spectra that will be added to the experimental data as input to the ML algorithms to recreate $\mu_a(\lambda)$ and obtain precise diagnostic information. We also plan to test different algorithms in the GANs models to check if they bring better accuracy in the generated spectra than the ones used in the present study. After performing such tests and if diseased brain tissues become available for study, we plan to perform similar studies with those tissues to retrieve the pigments, DNA and hemoglobin contents. By comparing those contents between healthy and diseased brain tissues, we can provide precise diagnostic information or even establish a relation between those contents and the progression of the disease for early detection procedures to be developed.

Disclosures

All authors declare that there is no conflict of interests in this paper.

Acknowledgements

References

1. S. Carvalho, I. Carneiro, R. Henrique, V. Tuchin, and L. Oliveira, "Lipofuscin-type pigment as a marker of colorectal cancer," Electronics 9(11), 1805 (2020).
2. L. Fernandes, S. Carvalho, I. Carneiro, R. Henrique, V. V. Tuchin, H. P. Oliveira, and L. M. Oliveira, "Diffuse reflectance and machine learning to differentiate colorectal cancer," Chaos 31, 053118 (2021).
3. L. M. Oliveira. K. I. Zaytsev, and V. V. Tuchin, "Improved biomedical imaging over a wide spectral range from UV есл to THz towards multimodality," SPIE Proceedings 11585, 1158503 (2020).
4. D. K. Tuchina, A. N. Bashkatov, A. B. Bucharskaya, E. A. Genina, and V. V. Tuchin, "Study of glycerol diffusion in skin and myocardium ex vivo under the conditions of developing alloxan-diabetes," Journal of Biomedical Photonics & Engineering 3(2), 020302 (2017).
5. D. K. Tuchina, R. Shi, A. N. Bashkatov, A. A. Genina, D. Zhu, Q. Luo, and V. V. Tuchin, "Ex vivo optical measurements of glucose diffusion kinetics in native and diabetic mouse skin," Journal of Biophotonics 8(4), 332–346 (2015).
6. K. Wakamatsu, T. Murase, F. A. Zucca, and S. Ito, "Biosynthetic pathway to neuromelanin and its aging process," Pigment Cell & Melanoma Research 25(6), 792–803 (2012).
7. J. K. Reddy, N. D. Lalwani, M. K. Reddy, and S. A. Qureshi, "Excessive accumulation of autofluorescence lipofuscin in the liver during hepatocarcinogenesis by methyl clofenapate and other hypolipidemic peroxisome proliferators," Cancer Research 42(1), 259–266 (1982).
8. Y. Kakimoto, C. Okada, N. Kawabe, A. Sasaki, H. Tsukamoto, R. Nagao, and M. Osawa, "Myocardial lipofuscin accumulation in ageing and sudden cardiac death," Scientific Reports 9(1), 3304 (2019).
9. G. Zonios, L. T. Perelman, V. Backman, R. Manoharan, M. Fitzmaurice, J. Van Dam, and M. S. Feld, "Diffuse reflectance spectroscopy of human adenomatous colon polyps in vivo," Applied Optics 38(31), 6628–6637 (1999).
10. N. Gomes, V. V. Tuchin, and L. M. Oliveira, "Refractive index matching efficiency in colorectal mucosa treated with glycerol," IEEE Journal of Selected Topics in Quantum Electronics 27(4), 7200808 (2021).
11. N. Gomes, V. V. Tuchin, and L. Oliveira, "UV-NIR efficiency of the refractive index matching mechanism on colorectal muscle during treatment with different glycerol osmolarities," Journal of Biomedical Photonics & Engineering 6(2), 020307 (2020).
12. I. Carneiro, S. Carvalho, R. Henrique, L. Oliveira and V. V. Tuchin, "Measurement of optical properties of normal and pathological human liver tissues from deep-UV to NIR," SPIE Proceedings 11363, 11363G (2020).
13. T. M. Gonçalves, I. S. Martins, H. F. Silva, V. V. Tuchin, and L. M. Oliveira, "Spectral optical properties of rabbit brain cortex between 200 and 1000 nm," Photochem 1(2), 190–208 (2021).
14. I. S. Martins, Caracterização das Propriedades Óticas do Pâncreas e Estudo da Difusão da Glicerina no seu Interior, MsC thesis, Polytechnic Institute of Porto – School of Engineering, Porto, Portugal, June 30 (2021).
15. A. R. Botelho, Determinação das propriedades Óticas de Tecidos e Caracterização de Tratamentos de Transparência em Rim Humano Normal e Patológico, MsC thesis, Polytechnic Institute of Porto – School of Engineering, Porto, Portugal, November 15 (2021).
16. V. V. Tuchin, Tissue Optics – Light Scattering Methods and Instruments for Medical Diagnosis, 3rd ed., SPIE Press, Bellingham (WA), USA (2015).
17. L. Wang, S. L. Jacques, and L. Q. Zheng, "MCML-Monte Carlo modeling of light transport in multi-layered tissues," Computer Methods and Programs in Biomedicine 47(2), 131–146 (1995).
18. S. A. Prahl, M. J. C. van Gemert, and A. J. Welch, "Determining the optical properties of turbid media by using the adding-doubling method," Applied Optics 32(4), 559–568 (1993).
19. L. M. C. Oliveira, V. V. Tuchin, The Optical Clearing Method: A New Tool for Clinical Practice and Biomedical Engineering, Springer, Cham, Switzerland (2019). ISBN: 978-3-030-33055-2.
20. V. Backman, A. Wax, and H. Zhang, A Laboratory Manual in Biophotonics, CRC Press, Boca Raton, USA (2018).
21. P. Pradhan, S. Guo, O. Ryabchykov, J. Popp, and T. W. Blocklitz, "Deep learning a boom for biophotonics?" Journal of Biophotonics 13(6), e201960186 (2020).
22. A. Creswell, T. White, V. Dumoulin, K. Arulkumaran, B. Sengupta, and A. A. Bharath, "Generative Adversarial Networks: An overview," IEEE Signal Processing Magazine 35, 53 (2018).
23. I. Goodfellow, J. Pouget-Abadie, M. Mirza, B. Xu, D. Warde-Farley, S. Ozair, A. Courville, and Y. Bengio, "Generative adversarial networks," arXiv:1406.2661v1 (2014).
24. L. Lan, L. You, Z. Zhang, Z. Fan, W. Zhao, N. Zeng, Y. Chen, and X. Zhou, "Generative adversarial networks and its applications in biomedical informatics," Frontiers in Public Health 8, 164 (2020).
25. GBD 2016 Neurology Collaborators, "Global, regional, and national burden of neurological disorders, 1990-2016: A systemic analysis for the global burden of disease study 2016," The Lancet Neurology 18(5), 459–480 (2019).
26. M. P. Mattson, W. Duan, W. A. Pedersen, and C. Culmsee, "Neurodegenerative disorders and ischemic brain diseases," Apoptosis 6, 69–81 (2001).
27. K. L. Double, V. N. Dedov, H. Fedorov, E. Kettle, G. M. Halliday, B. Garner, and U. T. Brunk, "The comparative biology of neuromelanin and lipofuscin in the brain," Cellular and Molecular Life Sciences 65, 1669–1682 (2008).

28. A. Moreno-García, A. Kun, M. Calero, and O. Calero, "The neuromelanin paradox and its role in oxidative stress and neurodegeneration," Antioxidants 10(1), 124 (2021).

29. V. V. Tuchin, Optical Clearing of Tissues and Blood, SPIE Press, Bellingham (WA), USA (2006).

30. A. Y. Sdobnov, M. Darvin, E. A. Genina, A. N. Bashkatov, J. Lademan, and V. V. Tuchin, "Recent progress in tissue optical clearing for spectroscopic application," Spectrochimica Acta Part A: Molecular and Biomolecular Spectroscopy 197, 216–229 (2018).

31. T. Stewart, "Down the Rabbit Hole: Rabbit Brain vs Human Brain" (Accessed March 2022) [https://prezi.com/nmxefcgdiqq5/rabbit-brain-vs-human-brain/].

32. J. Johansson, "Spectroscopic method for determination of the absorption coefficient in brain tissue," Journal of Biomedical Optics 15(5), 057005 (2010).

33. E. P. Gilissen, L. Staneva-Dobrovski, "Distinct types of lipofuscin pigment in the hippocampus and cerebellum of aged cheirogaleid primates," The Anatomical Record 296(12), 1895–1906 (2013).

34. H. Heinsen, "Lipofuscin in the cerebellar cortex of albino rats: An electron microscopic study," Anatomy and Embryology 115, 333-345 (1979).

35. G. O. Ivy, S. Kanai, M. Ohta, G. Smith, Y. Sato, M. Kobayashi, and K. Kitani, "Lipofuscin-like substances accumulate rapidly in brain, retina and internal organs with cysteine protease inhibition," Advances in Experimental Medicine and Biology 266, 31–45 (1989).

36. J. D. Johansson, K. Wårdell, "Intracerebral quantitative chromophore estimation from reflectance spectra captured during deep brain stimulation implantation," Journal of Biophotonics 6, 435–445 (2013).

37. G. Zonios, A. Dimou, I. Bassukas, D. Galaris, A. Tsolakidis, and E. Kaxiras, "Melanin absorbance spectroscopy: new method for noninvasive skin investigation and melanoma detection," Journal of Biomedical Optics 13, 0140017 (2008).

38. M. B. Różanowska, A. Pawlak, and B. Różanowski, "Products of docosahexaenoate oxidation as contributors to photosensitizing properties of retinal lipofuscin," International Journal of Molecular Sciences 22(7), 3525 (2021).

39. G. D. Fasman, "Ultraviolet spectra of derivatives of cysteine, cysteine, histidine, phenylalanine, tyrosine, and tryptophan," Chapter 17 in Handbook of Biochemistry and Molecular Biology, G. D. Fasman (Ed.), 3rd ed., Volume 1, CRC Press, Boca Raton (FL), 192-199 (2018).

40. D. B. Wetlaufer, "Ultraviolet spectra of proteins and amino acids," Chapter 6 in Advances in Protein Chemistry, C. B. Afinsen Jr. (Ed.), Vol. 17, Academic Press, London, 303_390 (1963).

41. R. K. Narayan, W. E. Heydon, G. J. Creed, and D. M. Jacowitz, "Identification of major proteins in human cerebral cortex and brain tumors," Journal of Protein Chemistry 4(6), 375–389 (1985).

42. Y. Zhou, J. Yao, and L. V. Wang, "Tutorial on photoacoustic tomography," Journal of Biomedical Optics 21(6), 061007 (2016).

43. I.-E. Pralea, R.-C. Moldovan, A.-M. Petrache, M. Ilies, S.-C. Heghes, I. Ielciu, R. Nicoară, M. Moldovan, M. Ene, M. Radu, A. Uifălean, and C.-A. Iuga, "From extraction to advanced analytical methods: The challenges of melanin analysis," International Journal of Molecular Sciences 20(16), 3943 (2019).

44. S. L. Jacques, "Extinction Coefficient of Melanin," (Accessed March 2022) [https://omlc.org/spectra/melanin/extcoeff.html].

45. L. Zhang, X. Zou, B. Zhang, L. Cui, J. Zhang, Y. Mao, L. Chen, and M. Li, "Label-free imaging of hemoglobin degradation and hemosiderin formation in brain tissues with femtosecond pump-probe microscopy," Theranostics 8(15), 4129–4140 (2018).

46. K. Zaghdoudi, O. Ngomo, R. Vanderesse, P. Anoux, B. Myszakhmetov, C. Frochot, and Y. Guiavarch, "Extraction, identification and photo-physical characterization of persimmon (Diospyros kaki L.) carotenoids," Foods 6(1), 4 (2017).

47. A. S. Raja, J. Sathiyabama, R. Venkatesan, and V. Prathipa, "Corrosion control of carbon steel by eco-friendly inhibitor L-Cysteine-Zn2+ system in aqueous medium," Journal of Chemical, Biological and Physical Sciences 4(4), 3182–3189 (2014).

48. C. Hazra, T. Samantha, and V.A. Mahalingham, "A resonance energy transfer approach for the selective detection of aromatic amino acids," Journal of Materials Chemistry C 2(47), 10157–10163 (2014).

49. J. H. Lin, C.-J. Yu, Y.-C. Yang, and W.-L. Tseng, "Formation of fluorescence polydopamine dots from hydroxyl radical-induced degradation of polydopamine nanoparticles," Physical Chemistry Chemical Physics 17(23), 15124–15130 (2015).

50. S. Feng, T. Harayama, S. Montessuit, F. P. A. David, N. Winssinger, J.-C. Martinou, and H. Riezman, "Mitochondria-specific photoactivation to monitor local sphingosine metabolism and function," Elife 7, e34555 (2018).